ACS APPLIED MATERIALS & INTERFACES

Research Article

www.acsami.org

Uniform PEGylated PLGA Microcapsules with Embedded Fe_3O_4 Nanoparticles for US/MR Dual-Modality Imaging

Sijia Xu,[†,§] Fei Yang,[†,§] Xiao Zhou,[‡] Yaping Zhuang,[†] Baoxia Liu,[†] Yang Mu,[‡] Xing Wang,[†] Hong Shen,[†] Guang Zhi,[‡] and Decheng Wu*[,†]

[†]Beijing National Laboratory for Molecular Sciences, State Key Laboratory of Polymer Physics and Chemistry, Institute of Chemistry, Chinese Academy of Sciences, Beijing 100190, China

[‡]Department of Cardiology, Chinese PLA General Hospital, Beijing 100853, China

ABSTRACT: Well-designed agents for enhanced multimodal imaging have attracted great interests in recent years. In this work, we adopted a premix membrane emulsification (PME) method to prepare uniform PEGylated poly(lactic-*co*-glycolic acid) (PLGA) microcapsules (MCs) with superparamagnetic Fe_3O_4 nanoparticles (NPs) embedded in the shell (Fe_3O_4@PEG−PLGA MCs) for ultrasound (US)/magnetic resonance (MR) bimodal imaging. Compared to Fe_3O_4@PLGA MCs without PEGylation, Fe_3O_4@PEG−PLGA MCs could more stably and homogeneously disperse in physiological solutions. *In vitro* and *in vivo* trials demonstrated that Fe_3O_4@PEG−PLGA MCs (~3.7 μm) with very narrow size distribution (PDI = 0.03) could function as efficient dual-modality contrast agents to simultaneously enhance US and MR imaging performance greatly. *In vitro* cell toxicity and careful histological examinations illustrated no appreciable cytotoxicity and embolism of Fe_3O_4@PEG−PLGA MCs to mice even at high dose. The uniform composite MCs developed here can act as clinical bimodal contrast agents to improve hybrid US/MR imaging contrast, which is promising for accurate diagnosis and real-time monitoring of difficult and complicated diseases.

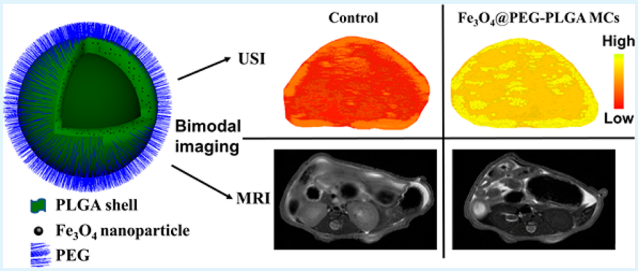

KEYWORDS: *Fe_3O_4 nanoparticles, PEG−PLGA microcapsules, contrast agents, ultrasound imaging, magnetic resonance imaging*

INTRODUCTION

Ultrasound imaging (USI) and magnetic resonance imaging (MRI) are two common imaging methods used in clinic for their noninvasive and nonradiative properties.[1,2] USI possesses a number of advantages, such as multifunction, low cost, portability, and real-time imaging, but its application is bounded due to the drawbacks including poor bone penetrability, gas barrier, low resolution, and so on.[3] In contrast, MRI can offer excellent resolution for soft tissues, but it is easily influenced by metals, combined with high cost and long imaging period.[4] Usually, only USI or MRI cannot provide enough physiological information for accurate diagnosis of miscellaneous difficult and complicated cases, for example, cancer, cardiovascular, and neurological diseases.[5] Since USI and MRI can perform complementary functions,[6] integration of these two imaging methods is a popular solution to achieve more abundant pathological information for accurately diagnosing complicated diseases.[7,8]

On various occasions, the contrasts of USI and MRI are not high enough to get a clear image,[9,10] so contrast agents are needed to enhance the contrast so as to obtain a distinct image.[11,12] At present, only single-modality contrast agents in clinic are available to enhance USI or MRI. To achieve effective both USI and MRI, a usual method is to inject these two kinds of contrast agents, respectively. However, the method not only increases the pain and cost, but also aggravates the metabolic burden of body. Besides, there may be repulsion and quenching effect between these two kinds of contrast agents with quite different biodistribution, discouraging the fusion of USI and MRI.[13,14] Hence, it is of great clinical significance to exploit dual-modality US/MR imaging contrast agents for diagnosis, location, monitoring, and evaluation of diseases.[15]

Gas-filled microcapsules (MCs) with a diameter of 2−8 μm are generally used as contrast agents for USI due to their ascendant scattering properties compared with the surrounding fluid.[16] Recently, magnetic iron oxide nanoparticles (NPs) or Gd agents were loaded in MCs to achieve dual-modality US/MR imaging contrast agents.[17−26] Gätjens et al. prepared iron oxide NPs-embedded poly(butyl cyanoacrylate) MCs for US/MR dual-modality imaging through a one-pot emulsion polymerization,[27] while Chen et al. developed iron oxide NPs-stabilized polymer nanocapsules via a single-step emulsion process to implement similar functions.[28] Zheng et al. generated superparamagnetic iron oxide NPs loaded MCs made of poly(lactic-*co*-glycolic acid) (PLGA) via a W/O/W double emulsion to serve as dual-modality contrast agents, enhancing USI and MRI simultaneously.[29−32] In spite of the above-mentioned encouraging results, most of previously

Received: July 21, 2015
Accepted: August 26, 2015
Published: August 26, 2015

DOI: 10.1021/acsami.5b06594
ACS Appl. Mater. Interfaces 2015, 7, 20460−20468

Scheme 1. Schematic of (B) a PME Method Generating Uniform MCs via the Microporous Membrane Compared to (A) a Traditional Water/Oil/Water Method Yielding MCs with a Broad Size Distribution. (C) Typical Structure of a Fe_3O_4@PEG−PLGA MC Containing a Cavity, a Fe_3O_4 Embedded PLGA Shell, and PEG Modified Surface

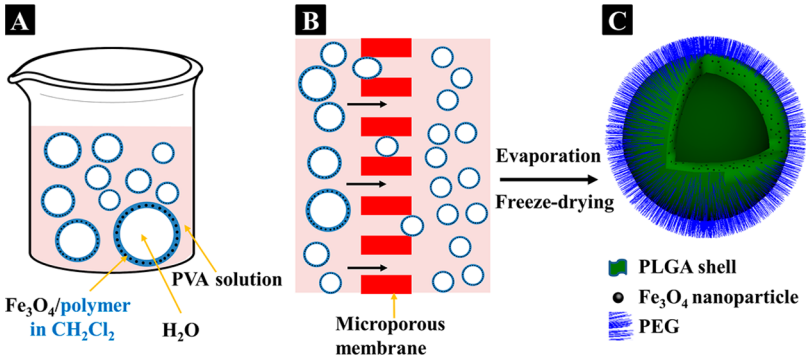

reported composite MCs for US/MR dual-modality imaging were beyond the optimized diameter of 2−8 μm and short of careful surface modification to heighten USI. These MCs might not have the optimal performance for USI, particularly *in vivo* because the MCs without surface modification would most possibly be recognized as foreign matters and engulfed by macrophages, which shortened their lifetime *in vivo* greatly.[33] In addition, the size distribution of most MCs reported was not narrow enough, resulting in biosafety issue *in vivo*. In other words, the uncontrolled large MCs easily lead to pulmonary embolism during circulation after injection *in vivo*.[34] It is therefore of great desire for development of surface modified composite MCs with narrow size distribution to greatly enhance US/MR dual-modality imaging with long duration and avoid the potential unsafety *in vivo*.

Biodegradable polyesters like polyhydroxyalkanoates and PLGA are widely used as biomaterials owing to their low toxicity to the organism.[35−41] PLGA is a FDA-approved material widely used as drug carriers and tissue engineering matrices because of adjustable degradation rate, mechanical property, and good processability.[39−41] Herein, we prepared uniform PEGylated PLGA microcapsules with superparamagnetic Fe_3O_4 NPs embedded in the shell (Fe_3O_4@PEG−PLGA MCs) via a premix membrane emulsification (PME) method (Scheme 1B), which was first used in our recent report to develop polylactone MCs with even sizes for USI.[39] The obtained Fe_3O_4@PEG−PLGA MCs can serve as contrast agents for dual-modality US/MR imaging. Both USI and MRI contrast behaviors of Fe_3O_4@PEG−PLGA MCs as well as their biosafeties were evaluated *in vitro* and *in vivo*.

EXPERIMENTAL SECTION

Materials. Ferric acetylacetonate ($Fe(acac)_3$), 1,2-hexadecanediol, oleylamine, oleic acid, benzyl ether, polyethylene glycol (PEG), and paclitaxel (PTX) were purchased from J&K Scientific Ltd. Glycolide and lactide were purchased from Purac (Netherlands) and further purified by recrystallization from ethyl acetate twice. Stannous octoate (A.R.), poly(vinyl alcohol) (PVA), evans blue, and fluorescein diacetate were purchased from Sigma-Aldrich. Premix membrane emulsification equipment (FMEM-500M) and Shirasu porous glass (SPG) membrane were purchased from National Engineering Research Center for Biotechnology (Beijing). The glass membranes were annular cylinders (inner diameter = 8 mm, external diameter = 10 mm, length = 170 mm) with pore sizes of 7.2 μm. Other compounds and solvents were purchased from Beijing Chemical Reagents Company, China.

Synthesis and Characterization of Fe_3O_4 NPs. *Synthesis of 4 nm Fe_3O_4 NPs.* Fe_3O_4 NPs were synthesized in terms of the previous literature with minor modification.[42] $Fe(acac)_3$ (1 mmol), 1,2-hexadecanediol (6 mmol), oleylamine (3 mmol), oleic acid (3 mmol), and phenyl ether (15 mL) were mixed with magnetic stirring under a flow of argon, followed by heating to 210 °C in an argon atmosphere. After being maintained at 210 °C for 45 min, the mixture was heated to reflux (~270 °C) for another 45 min, presenting from red−brown to black−brown. It was then cooled to room temperature via removal of the heat source. Under ambient conditions, black products were precipitated from the mixture by adding ethanol (50 mL) to it, followed by separation via centrifugation. The black products were dissolved in hexane along with oleic acid (0.02 mL) and oleylamine (0.02 mL). Centrifugation (3K30, Sigma) was applied (11 000 rpm, 8 min) to get rid of any undispersed residue. Four nanometer Fe_3O_4 NPs were obtained by precipitation with addition of ethanol to the supernate and redispersed into hexane for further use after centrifugation (11 000 rpm, 8 min).

Synthesis of 6 nm Fe_3O_4 NPs. $Fe(acac)_3$ (1 mmol), 1,2-hexadecanediol (6 mmol), oleylamine (3 mmol), oleic acid (3 mmol), and benzyl ether (15 mL) were mixed with magnetic stirring under a flow of argon, followed by heating to 210 °C in an argon atmosphere. After being maintained at 210 °C for 2 h, the mixture was heated to reflux (~310 °C) for 1 h, presenting from red−brown to black−brown. It was then cooled to room temperature via removal of the heat source. Following the post processing in the preparation of 4 nm Fe_3O_4 NPs, 6 nm Fe_3O_4 NPs dispersed in *n*-hexane were produced.

Synthesis of 8 nm Fe_3O_4 NPs. $Fe(acac)_3$ (1 mmol), 1,2-hexadecanediol (6 mmol), oleylamine (3 mmol), oleic acid (3 mmol), phenyl ether (15 mL), and *n*-hexane dispersion (3 mL) of 6 nm Fe_3O_4 NPs (40 mg) were mixed with magnetic stirring under a flow of argon, followed by heating to 100 °C to remove hexane. After being maintained at 100 °C for 1 h, the mixture was heated to reflux (~270 °C) for 1 h in an argon atmosphere. The black-colored mixture was cooled to room temperature by removing the heat source. It was then cooled to room temperature via removal of the heat source. Following the post processing in the preparation of 4 nm Fe_3O_4 NPs, 8 nm Fe_3O_4 NPs dispersed in *n*-hexane were produced.

Characterization. Transmission electron microscopy (TEM) images of Fe_3O_4 NPs were captured on a JEOL 2100F electron microscopy with an acceleration voltage of 200 kV. X-ray diffraction (XRD) patterns of Fe_3O_4 NPs were recorded by a Rigaku D/max 2500 diffractometer equipped with Cu-target.

Synthesis and Characterization of PLGA and PEG-*b*-PLGA. PLGA7030 was synthesized via ring-opening polymerization of L-lactide and glycolide (n_{LA}:n_{GA} = 70:30). Typically, rigorously dried lactide (70 mmol), glycolide (30 mmol), hexadecanol (0.14 mmol), and stannous octoate (0.05 wt % of lactide and glycolide) were transferred into a polymerization tube. After being purged with argon three times, the tube was sealed in vacuum. Then the tube was heated to 170 °C for 20 h. The obtained product was dissolved in chloroform, then precipitated into ethanol, followed by drying under vacuum at 35

DOI: 10.1021/acsami.5b06594
ACS Appl. Mater. Interfaces 2015, 7, 20460−20468

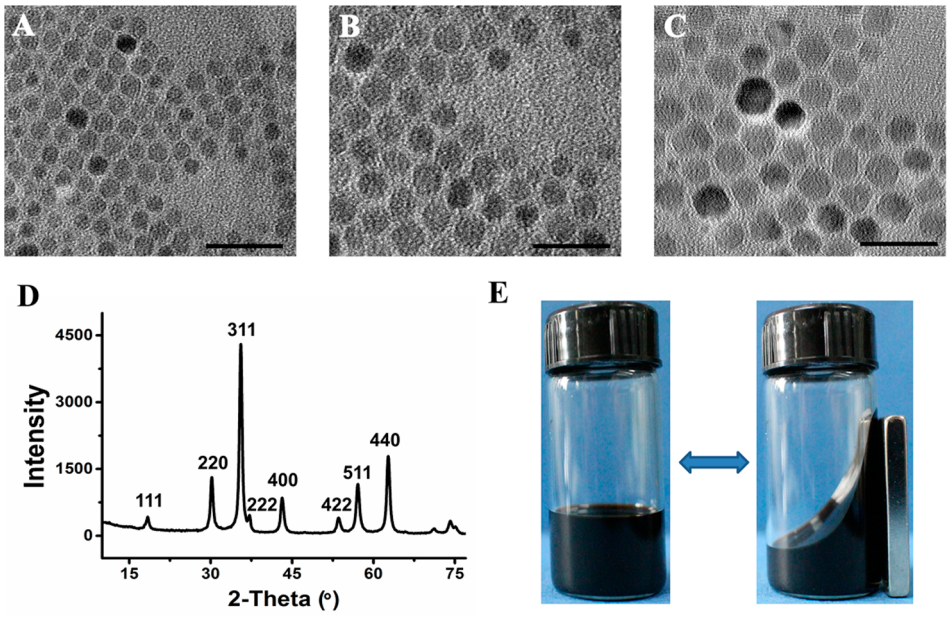

Figure 1. Characterization of Fe_3O_4 NPs. TEM images of (A) 4 nm (<D> = 4.0 ± 0.2 nm), (B) 6 nm (<D> = 5.9 ± 0.3 nm), and (C) 8 nm (<D> = 8.0 ± 0.4 nm) Fe_3O_4 NPs. Scale bar is 20 nm. The number of counted particles was 40. (D) XRD pattern of 6 nm Fe_3O_4 NPs. (E) Hydromagnetic property of 6 nm Fe_3O_4 NPs dispersed in *n*-hexane.

°C to achieve a constant weight. PEG-*b*-PLGA7030 was synthesized similarly using PEG (Mw = 5000) as an initiator instead of hexadecanol. To determine average molecular weight of the polymers, gel permeation chromatography (GPC, max VE-2001, Viscotek) measurement based on polystyrene standards was performed with chloroform as the eluent at a flow rate of 1.0 mL/min. The GPC results of the synthesized polymers were as follows: PLGA7030 (M_w = 85000, M_w/M_n = 1.21), and PEG-*b*-PLGA7030 (M_w = 86,000, M_w/M_n = 1.23).

Preparation and Characterization of MCs. Fe_3O_4@PEG−PLGA MCs were prepared via a two-step approach. First, to ensure homogeneous dispersion of Fe_3O_4 nanoparticles in dichloromethane dissolving PEG−PLGA, *n*-hexane with Fe_3O_4 NPs dispersed was added to dichloromethane dissolving PEG−PLGA under stirring. After the solvent was removed via reduced pressure distillation, the remained solid was redispersed by dichloromethane. Four milliliters of water was mixed with 6 mL of the obtained dichloromethane containing 300 mg of PEG−PLGA and varying amount of Fe_3O_4 NPs under sonication to form an elementary emulsion. Second, the W/O emulsion was poured into aqueous external phase containing 1 wt % PVA with magnetic stirring for 120 s at 800 rpm to generate coarse double emulsions, which were then homogenized by squeezing them through the SPG membrane under a pressure of 90 kPa. The yielded uniform double emulsion was transferred quickly into 600 mL of deionized water with magnetic stirring (500 rpm, 24 h) to solidify the Fe_3O_4@PEG−PLGA MCs. The obtained Fe_3O_4@PEG−PLGA MCs were collected via centrifugation (3000 rpm, 5 min) and washed by deionized water three times, followed by freeze-drying in a lyophilizer (ALPHA 1−2 LD, Christ) to sublimate the encapsulated frozen water. The resulting loose powder was stored at 2 °C for further use.

Fe_3O_4@PLGA MCs were prepared similarly by substituting PEG−PLGA with PLGA. Pure PEG−PLGA MCs were fabricated similarly without the addition of Fe_3O_4 NPs.

After the MCs were coated with gold palladium by sputter coater (E-1010; Hitachi) under vacuum, they were observed by scanning electron microscopy (SEM, JSM-6700F, JEOL) with an accelerating voltage of 5 kV. The existence of Fe_3O_4 NPs in the MCs was confirmed by energy dispersive X-ray (EDX) spectrum at 15 kV. The Fe_3O_4-inclusion weight contents of MCs were determined by inductively coupled plasma mass spectrometry (ICP-MS, element, Finnigan). The size distribution of MCs dispersed in distilled water was measured via dynamic light scattering (DLS) method using a zetasizer (Nano ZS90, Malvern). The magnetic properties of MCs were characterized by using a vibrating sample magnetometer (VSM, 7410, Lake Shore Cryotronics) at 37 °C.

***In Vitro* USI and MRI.** *In vitro* USI was carried out under flow state to simulate blood circulation. A silicone tube (inner diameter = 3 mm, external diameter = 6 mm) was set in a tank filled with degassed water. MCs were evenly dispersed in degassed water. The resulting MCs dispersion was flew with a stable rate in the tube, which was captured by an ultrasonic imaging machine (Acuson Sequoia 512 system, Siemens) in B mode with 10 MHz ultrasound probe. All USI experiments were under the same parameters (Mechanical Index, MI = 0.49) and repeated three times.

In vitro T_2-weighted MRI was acquired using a 7-T experimental MRI instrument (BioSpec 70/20 USR, Bruker). Homogeneous dispersions of MCs in normal saline with predetermined concentrations were placed in a series of tubes for T_2-weighted MRI. After careful preparation, the tubes were scanned in a 7-T MRI system.

***In Vivo* USI and MRI.** After anesthetized with chloral hydrate (10 wt %), 6-week-old nude mice were injected via tail vein using a syringe with 250 μL of normal saline, 250 μL of normal saline containing 0.6 mg of Fe_3O_4@PLGA MCs or 250 μL of normal saline containing 0.6 mg of Fe_3O_4@PEG−PLGA MCs. Their livers were imaged by an USI machine (Acuson Sequoia 512 system, Siemens) in B mode with 10 MHz ultrasound probe (MI = 0.49). After USI, *in vivo* MRI was performed immediately. T_2-weighted MR images of injected mice were acquired by using a 7-T experimental MRI instrument (BioSpec 70/20 USR, Bruker). Imaging parameters were set as follows: repetition time (TR) = 3000 ms; echo time (TE) = 40.6 ms; field of view (FOV) = 35 mm × 35 mm, slice thickness = 1 mm.

***In Vitro* Cell Toxicity.** Mouse embryonic fibroblasts (NIH/3T3) were used to evaluate *in vitro* cell toxicities of MCs. The cells were cultured in α-MEM supplemented with 10% fetal bovine serum in an atmosphere of 5% CO_2 at 37 °C. After sterilized by 70% ethanol solution for 40 min, various MCs with desired weight were transferred into wells of 96-well culture plate, respectively. Then, 80 μL of cell suspension with 1 × 10^5 cells was seeded into each well. After cell-seeded MCs were maintained under 5% CO_2 at 37 °C for 3 h, 240 μL of culture medium was added to each well. The viability and proliferation of NIH/3T3 cells cultured together with microcapsules for 1, 3, and 6 days were determined by CCK-8 assay. At each predetermined interval, the original culture medium in each well was removed, followed by the addition of fresh culture medium (100 μL).

DOI: 10.1021/acsami.5b06594
ACS Appl. Mater. Interfaces 2015, 7, 20460−20468

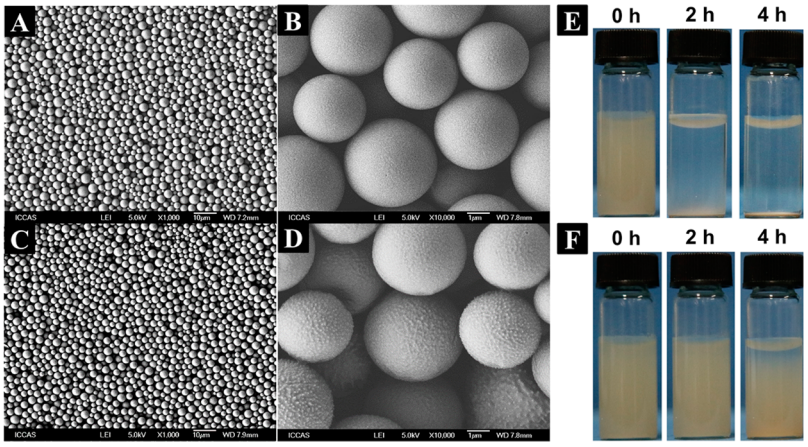

Figure 2. Morphologies of the composite MCs. (A) Low and (B) high magnification SEM images of Fe_3O_4@PLGA MCs. (C) Low and (D) high magnification SEM images of Fe_3O_4@PEG−PLGA MCs. Optical photos of (E) Fe_3O_4@PLGA MCs and (F) Fe_3O_4@PEG−PLGA MCs after being dispersed in normal saline for 2 and 4 h. The concentrations both are 3 mg/mL.

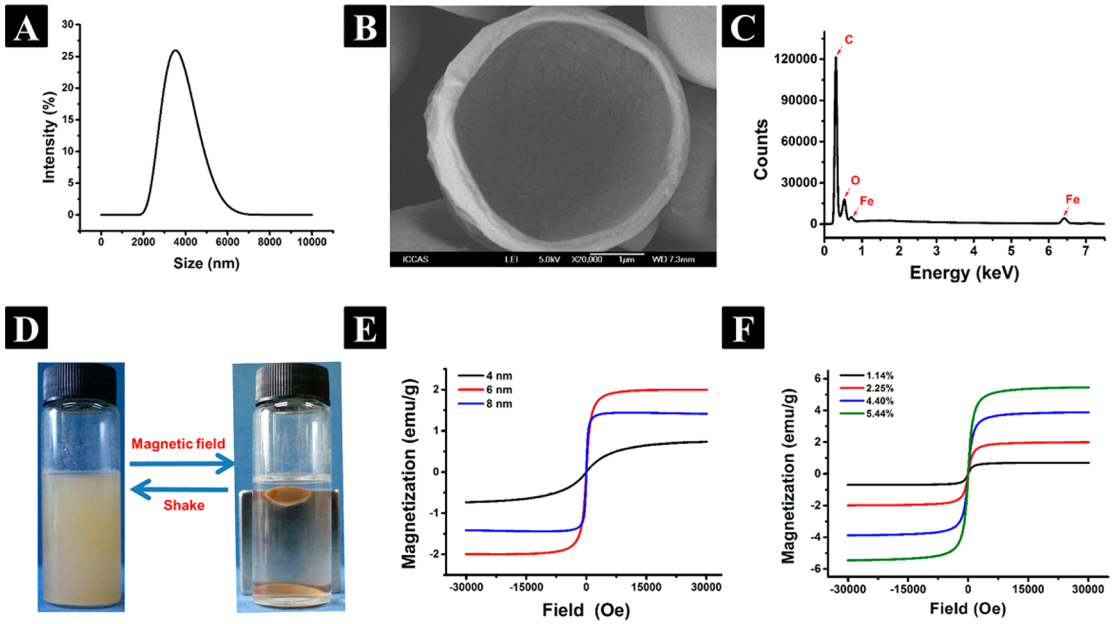

Figure 3. Characterization of Fe_3O_4@PEG−PLGA MCs. (A) Size distribution of Fe_3O_4@PEG−PLGA MCs. (B) SEM image of a Fe_3O_4@PEG−PLGA MC cut by a super thin blade. (C) EDX spectrum of Fe_3O_4@PEG−PLGA MCs. (D) Magnetic property of Fe_3O_4@PEG−PLGA MCs. (E) Hysteresis loops of 4, 6, and 8 nm Fe_3O_4 NPs embedded PEG−PLGA MCs. (F) Hysteresis loops of Fe_3O_4@PEG−PLGA MCs with different weight contents of 6 nm Fe_3O_4 NPs.

After CCK-8 solution (10 μL) was added to each well, NIH/3T3 cells were incubated at 37 °C under 5% CO_2 for 4 h. The absorbance of the culture medium was measured at 450 nm using microplate reader (ZS-2).

Histology Analysis. Two-hundred-fifty microliters of normal saline containing 1.2 mg of Fe_3O_4@PEG−PLGA MCs was injected intravenously into the nude mice through the tail vein. The mice were anatomized after 3 h, 3 days, and 30 days, respectively. The tissues including heart, liver, spleen, lung, and kidney were collected and fixed in 10% neutral buffered formalin. The tissues of controls were gained similarly without any injection. Then, the collected tissues were embedded in paraffin, sectioned (4 mm thick), and stained with hematoxylin and eosin (H&E). The histological sections were observed under an optical microscope.

Statistical Analysis. All tests were repeated thrice. Differences among the experimental groups were evaluated by a standard Student's *t*-test. *P*-values less than 0.05 were considered statistically significant.

RESULTS AND DISCUSSION

Synthesis and Characterization of Fe_3O_4 NPs. The sizes of Fe_3O_4 NPs have a significant effect on their magnetic property, and the composite MCs with various Fe_3O_4 NPs embedded have different performances for MRI imaging. To obtain the optimal size of Fe_3O_4 NPs, three kinds of Fe_3O_4 NPs with the sizes to be 4, 6, and 8 nm were prepared for further use through high-temperature reaction of ferric triacetylacetonate ($Fe(acac)_3$), 1,2-hexadecanediol. Wherein, 4 and 6 nm Fe_3O_4 NPs were yielded by varying the reaction temperature, while 8 nm Fe_3O_4 NPs were obtained by seed-mediated growth with 6 nm Fe_3O_4 NPs as seeds. TEM images (Figure 1A−C) show that the Fe_3O_4 NPs obtained were nearly monodisperse. The XRD pattern (Figure 1D) discloses that all diffraction peaks matched well with standard powder diffraction data of Fe_3O_4 NPs in position and relative intensity. The dispersion of Fe_3O_4

DOI: 10.1021/acsami.5b06594
ACS Appl. Mater. Interfaces 2015, 7, 20460−20468

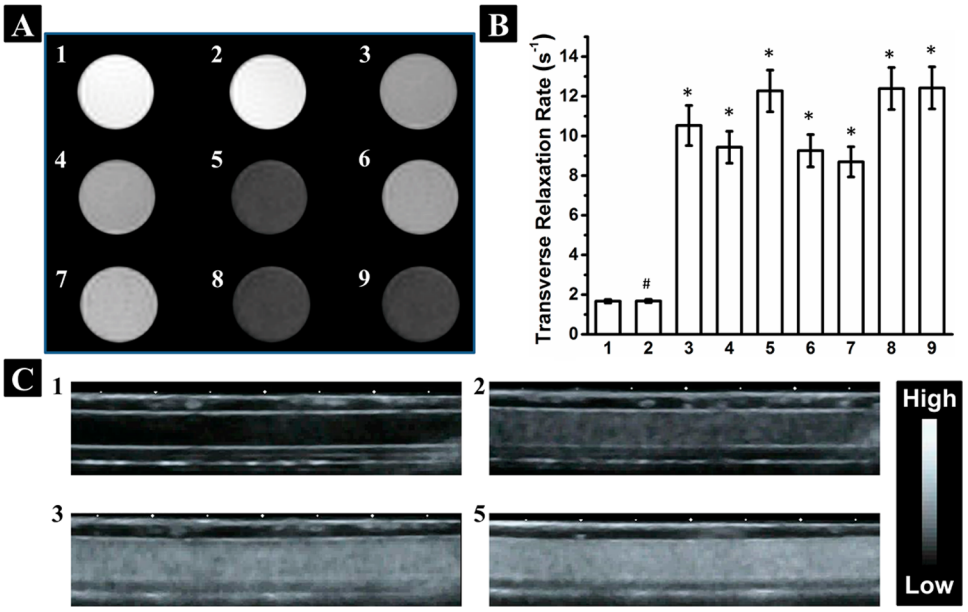

Figure 4. *In vitro* US/MR dual-modality images of various samples. (1) Normal saline; (2) PEG−PLGA MCs; (3) PLGA MCs with 2.25 wt % of 6 nm Fe_3O_4 NPs embedded; PEG−PLGA MCs with 2.25 wt % of (4) 4 nm, (5) 6 nm, and (6) 8 nm Fe_3O_4 NPs embedded; PEG−PLGA MCs with (7) 1.14 wt %, (8) 4.40 wt %, and (9) 5.44 wt % of 6 nm Fe_3O_4 NPs embedded. Concentrations of all MCs are 1 mg/mL. (A) *In vitro* MR images and (B) Transverse relaxation rate of samples 1−9. *, $p < 0.05$, significant against sample 1. #, $p > 0.05$, insignificant against sample 1. (C) *In vitro* US images of samples 1, 2, 3, and 5.

NPs in *n*-hexane was highly stable and performed as a magnetic fluid response to an external magnetic field (Figure 1E), indicating the Fe_3O_4 NPs could homogeneously disperse in *n*-hexane.

Design, Preparation, and Characterization of Fe_3O_4@PEG−PLGA MCs. It is reported that narrowly distributed MCs with suitable sizes (~4 μm) can achieve excellent USI performance as well as improved biosafety.[39] To obtain uniform microcapsules, we adopt a PME method instead of a traditional W/O/W method as indicated in Scheme 1, panel B. For the optimized performance *in vivo*, PEG-*b*-PLGA7030 was synthesized to prepare the composite MCs with PEGylated surface as illustrated in Scheme 1, panel C. Compared with the smooth surfaces of Fe_3O_4@PLGA MCs (Figure 2B), Fe_3O_4@PEG−PLGA MCs (Figure 2D) had rough surfaces due to gathering of PEG segments. The peripheral PEG segments made Fe_3O_4@PEG−PLGA MCs more stable in normal saline than Fe_3O_4@PLGA MCs as reflected in that almost all the Fe_3O_4@PLGA MCs precipitated from their dispersion within 2 h, while no significant aggregation was observed for the dispersion of Fe_3O_4@PEG−PLGA MCs 4 h later (Figure 2E,F).

Fe_3O_4@PEG−PLGA MCs had a mean diameter of 3.7 μm with a narrow size distribution of 0.03 (Figure 3A). To observe their inner structures, Fe_3O_4@PEG−PLGA MCs were cut by super thin razor blade, followed by imaging using SEM. Figure 3, panel B indicates the cut Fe_3O_4@PEG−PLGA MC was a bowl-like hemisphere with an about 100 nm-thick shell, demonstrating that the obtained Fe_3O_4@PEG−PLGA MCs possessed a hollow core/shell structure. The hollow core/shell structure could strengthen backscattering signals resulting in the contrast enhancement for USI. Fe, O, and C signals were observed from energy dispersive X-ray (EDX) spectrum of the MC surface in Figure 3, panel C, which was in accordance with the chemical signals of Fe_3O_4@PEG−PLGA MCs. Figure 3, panel D indicates that, when exposed to an external magnetic field, Fe_3O_4@PEG−PLGA MCs aggregated at the high-field site due to the intrinsic magnetic properties of embedded Fe_3O_4 NPs. After the magnet was removed, Fe_3O_4@PEG−PLGA MCs could be well redispersed in normal saline again by shaking. No remnant magnetization observed from hysteresis loops of Fe_3O_4@PEG−PLGA MCs demonstrated that the MCs possess superparamagnetic characteristic, and it was beneficial for applications *in vivo* (Figure 3E).[43] With the same content of Fe_3O_4 NPs, 6 nm Fe_3O_4 NPs embedded PEG−PLGA MCs had the strongest saturated magnetization compared to 4 or 8 nm Fe_3O_4 NPs embedded PEG−PLGA MCs. As the content of Fe_3O_4 NPs increased, the saturated magnetization of Fe_3O_4@PEG−PLGA MCs strengthened accordingly (Figure 3F). Combinedly, these data provide sufficient evidence for successful encapsulation of Fe_3O_4 NPs into the shell of PEG−PLGA MCs.

***In Vitro* US/MR Dual-Modality Imaging.** The size and weight contents of Fe_3O_4 NPs are directly related to MRI performance of the composite MCs. To determine the suitable size and content, we prepared several Fe_3O_4@PEG−PLGA MCs with varied sizes and contents of Fe_3O_4 NPs for evaluation. As a comparison, Fe_3O_4@PLGA MCs without PEGylation and PEG−PLGA MCs without loaded Fe_3O_4 NPs were also produced. These samples were evenly dispersed in normal saline and analyzed by an experimental 7-T MRI instrument with normal saline as a control. The T_2-weighted MR images are revealed in Figure 4, panel A, and their corresponding relaxation rates are summarized in Figure 4, panel B. PEG−PLGA MCs presented nearly the same MRI behaviors with normal saline, indicating no contrast improvement for MRI. Fe_3O_4@PLGA MCs exhibited a quite dark MR image, demonstrating that inclusion of Fe_3O_4 NPs can significantly enhance performance of T_2-weighted MRI. Compared to Fe_3O_4@PLGA MCs, Fe_3O_4@PEG−PLGA MCs with same size and content of embedded Fe_3O_4 NPs generated darker MR image with higher relaxation rate. In other words,

DOI: 10.1021/acsami.5b06594
ACS Appl. Mater. Interfaces 2015, 7, 20460−20468

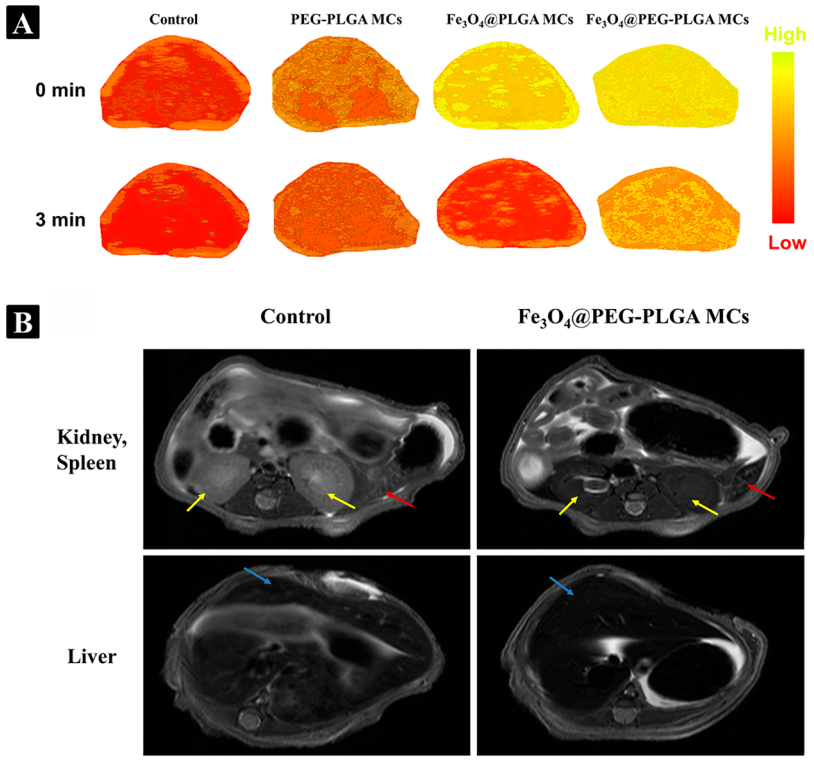

Figure 5. *In vivo* US/MR dual-modality imaging. (A) *In vivo* contrast-enhanced US images of mice liver after injection (top, 0 min; bottom, 3 min) of different samples. (B) *In vivo* MR images of nude mice after injection of Fe_3O_4@PEG−PLGA MCs. Yellow arrows indicate kidneys, red arrows indicate spleens, and blue arrows indicate livers. Control was performed by injection of normal saline.

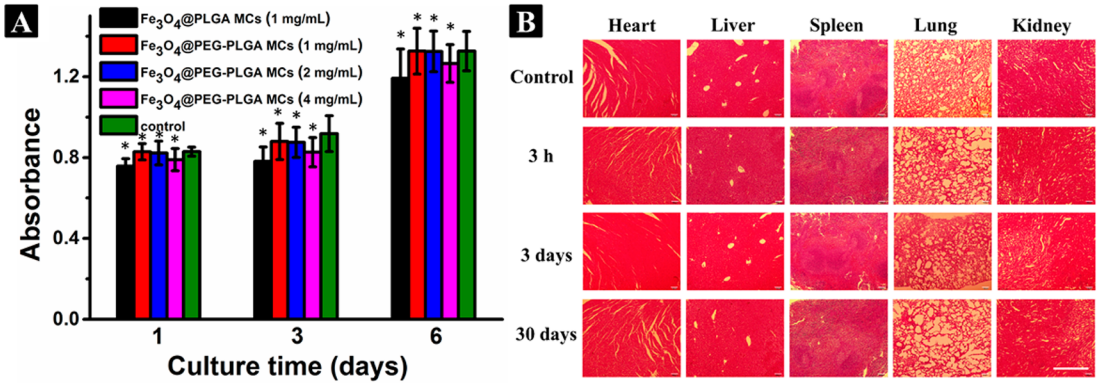

Figure 6. Biosafety evaluation of Fe_3O_4@PEG−PLGA MCs. (A) CCK-8 assay of NIH/3T3 cells incubated with Fe_3O_4@PLGA MCs and Fe_3O_4@PEG−PLGA MCs at various concentrations for different periods. Cells incubated without MCs were calculated as the control. ∗, $p > 0.05$, insignificant against the control. (B) Histological examination of nude mice at 3 h, 3 days, and 30 days after injection of Fe_3O_4@PEG−PLGA MCs. Their hearts, livers, spleens, lungs, and kidneys were stained by H&E. Untreated healthy nude mice were examined as the control. Scale bar is 500 μm.

Fe_3O_4@PEG−PLGA MCs possess better contrast enhancement for T_2-weighted MRI. The better MRI performance should ascribe to that Fe_3O_4@PEG−PLGA MCs have better stability in normal saline than do Fe_3O_4@PLGA MCs. With the same content of Fe_3O_4 NPs, 6 nm Fe_3O_4 NPs embedded PEG−PLGA MCs presented the strongest contrast enhancement for T_2-weighted MRI compared to 4 or 8 nm Fe_3O_4 NPs embedded PEG−PLGA MCs, which was consistent with the result of saturated magnetization as indicated in Figure 3, panel E. As the content of Fe_3O_4 NPs increased from 1.14 to 2.25 wt %, the transverse relaxation rate of Fe_3O_4@PEG−PLGA MCs increased from 8.6 to 12.3 S^{-1} accordingly. However, no significant improvement for T_2-weighted MRI was observed when the content was further raised to 4.40 and 5.44 wt %. Therefore, 2.25 wt % of 6 nm Fe_3O_4 NPs embedded PEG−PLGA MCs yielding good MRI performance were chosen for subsequent study *in vivo*.

To evaluate US contrast effect of Fe_3O_4@PEG−PLGA MCs, US images of the MCs dispersed in normal saline were captured under flow state simulating blood circulation. In comparison, USI behaviors of PEG−PLGA MCs and Fe_3O_4@PLGA MCs were also evaluated with normal saline as a control. Figure 4, panel C shows that PEG−PLGA MCs without embedded Fe_3O_4 NPs generated obviously enhanced ultrasound signals compared to normal saline. With introduction of Fe_3O_4 NPs, Fe_3O_4@PLGA and Fe_3O_4@PEG−PLGA compo-

DOI: 10.1021/acsami.5b06594
ACS Appl. Mater. Interfaces 2015, 7, 20460−20468

site MCs yielded much stronger ultrasound signals since the embedded Fe_3O_4 NPs highly enhances backscattering signals to US waves, which is in agreement with the previous reports.[26,29−31] Therefore, inclusion of Fe_3O_4 NPs can improve USI performance.

***In Vivo* US/MR Dual-Modality Imaging.** *In vivo* dual-modality imaging experiments were performed on nude mice to further assess the capacity of Fe_3O_4@PEG−PLGA MCs as US/MR contrast agents. From the color-coded US images of liver as shown in Figure 5, panel A,[44] obvious US contrast enhancement was observed from intravenously injected PEG−PLGA MCs, which did not degrade significantly after 3 min, indicating their long duration *in vivo*. Fe_3O_4@PLGA MCs exhibited stronger US contrast right after injection, which agrees with the result *in vitro*, but their contrast effect quickly dropped to nearly zero after 3 min. In contrast, integrating embedded Fe_3O_4 NPs and PEGylated surface, Fe_3O_4@PEG−PLGA MCs yielded excellent US contrast with long duration. Introduction of Fe_3O_4 NPs significantly enhanced US contrast, and PEGylated surface effectively prolongs their lifetime in blood circulation, averting phagocytosis by macrophages.

The T_2-weighted MR images of Fe_3O_4@PEG−PLGA MCs were acquired after USI trials as presented in Figure 5, panel B. A strong T_2-weighted contrast enhancement (dark image) was observed in kidney, spleen, and liver as indicated by arrows compared to the control, demonstrating that Fe_3O_4@PEG−PLGA MCs can act as excellent contrast agents in T_2-weighted MRI. It must be pointed out that the MRI experiment was performed right after USI evaluation without any new Fe_3O_4@PEG−PLGA MCs injected, confirming that Fe_3O_4@PEG−PLGA MCs have a great potentiality to serve as real dual-modality contrast agents for clinic applications.

Biosafety Evaluation. Although iron oxide (Fe_3O_4) NPs and PEG−PLGA have been approved to be used in clinic by FDA for their good biocompatibility,[45,46] it is still necessary to ensure the biosafety of PEG−PLGA MCs with Fe_3O_4 NPs embedded both *in vitro* and *in vivo*. We evaluated cytotoxicity of Fe_3O_4@PLGA MCs and Fe_3O_4@PEG−PLGA MCs in NIH/3T3 cells by measuring cell viability via CCK-8 assay. Figure 6, panel A shows that the number of the viable cells cultured with Fe_3O_4@PEG−PLGA MCs was nearly the same as that cultured with the control without MCs added when the concentrations of Fe_3O_4@PEG−PLGA MCs were 1 and 2 mg/mL. The number of the viable cells only slightly decreased even though the concentration was further increased to 4 mg/mL. Figure 6, panel A also indicates that NIH/3T3 cells can grow better with Fe_3O_4@PEG−PLGA MCs than Fe_3O_4@PLGA MCs. These results demonstrates that Fe_3O_4@PEG−PLGA MCs possess excellent cell compatibility and low cytotoxicity. To further investigate the potential toxicity *in vivo*, Fe_3O_4@PEG−PLGA MCs were injected into the nude mice at high dose, double that of the imaging dose. These nude mice lived as well as the healthy nude mice without injection for more than one month. Histological sections of their five major organs were stained with H&E. No appreciable embolism and histological changes were detected between the treated organs and normal organs (Figure 6B), proving Fe_3O_4@PEG−PLGA MCs having no harm to the mice. These results effectively evidence that Fe_3O_4@PEG−PLGA MCs should be safe for biomedical application.

CONCLUSION

Uniform Fe_3O_4@PEG−PLGA MCs with optimized size and content of embedded Fe_3O_4 NPs were successfully fabricated for US/MR dual-modality imaging. Synergistic interaction of PEGylated surface, embedded Fe_3O_4 NPs, and controlled even size is vital for this kind of composite MCs to achieve good USI/MRI performance as well as outstanding biocompatibility. Owing to the peripheral PEG segments, the Fe_3O_4@PEG−PLGA MCs exhibited good stability in normal saline and provided long blood circulation via greatly preventing them from phagocytosis by macrophages when applied *in vivo*. The Fe_3O_4@PEG−PLGA MCs (~3.7 μm, PDI = 0.03) could simultaneously enhance US and MR imaging contrast greatly both *in vitro* and *in vivo*. No appreciable cytotoxicity and embolism of Fe_3O_4@PEG−PLGA MCs to mice were observed even at high dose, illustrating that MCs possess excellent biocompatibility and biosafety. Considering that Fe_3O_4 NPs and PEG−PLGA are both FDA-approved materials used in clinic, this kind of Fe_3O_4@PEG−PLGA MCs has great potential to be further developed as efficient dual-modality contrast agents for practically biomedical application.

AUTHOR INFORMATION

Corresponding Author

*E-mail: dcwu@iccas.ac.cn.

Author Contributions

[§]These authors contributed equally to this work.

Notes

The authors declare no competing financial interest.

ACKNOWLEDGMENTS

We are grateful to MOST (2014CB932200 and 2014BAI11B04), NSFC (21174147 and 21474115), and the "Young Thousand Talents Program" for financial support.

REFERENCES

(1) Weissleder, R.; Mahmood, U. Molecular Imaging. *Radiology* **2001**, *219*, 316−333.

(2) Massoud, T. F.; Gambhir, S. S. Molecular Imaging in Living Subjects: Seeing Fundamental Biological Processes in a New Light. *Genes Dev.* **2003**, *17*, 545−580.

(3) Jokerst, J. V.; Khademi, C.; Gambhir, S. S. Intracellular Aggregation of Multimodal Silica Nanoparticles for Ultrasound-Guided Stem Cell Implantation. *Sci. Transl. Med.* **2013**, *5*, 177ra35.

(4) Zhang, B. B.; Li, Q.; Yin, P. H.; Rui, Y. P.; Qiu, Y. Y.; Wang, Y.; Shi, D. L. Ultrasound-Triggered BSA/SPION Hybrid Nanoclusters for Liver-Specific Magnetic Resonance Imaging. *ACS Appl. Mater. Interfaces* **2012**, *4*, 6479−6486.

(5) Lee, S. Y.; Jeon, S. I.; Jung, S.; Chung, I. J.; Ahn, C. H. Targeted Multimodal Imaging Modalities. *Adv. Drug Delivery Rev.* **2014**, *76*, 60−78.

(6) Pinto, P. A.; Chung, P. H.; Rastinehad, A. R.; Baccala, A. A., Jr.; Kruecker, J.; Benjamin, C. J.; Xu, S.; Yan, P.; Kadoury, S.; Chua, C.; Locklin, J. K.; Turkbey, B.; Shih, J. H.; Gates, S. P.; Buckner, C.; Bratslavsky, G.; Linehan, W. M.; Glossop, N. D.; Choyke, P. L.; Wood, B. J. Magnetic Resonance Imaging/Ultrasound Fusion Guided Prostate Biopsy Improves Cancer Detection Following Transrectal Ultrasound Biopsy and Correlates with Multiparametric Magnetic Resonance Imaging. *J. Urol.* **2011**, *186*, 1281−1285.

(7) Vourganti, S.; Rastinehad, A.; Yerram, N. K.; Nix, J.; Volkin, D.; Hoang, A.; Turkbey, B.; Gupta, G. N.; Kruecker, J.; Linehan, W. M.; Choyke, P. L.; Wood, B. J.; Pinto, P. A. Multiparametric Magnetic Resonance Imaging and Ultrasound Fusion Biopsy Detect Prostate

DOI: 10.1021/acsami.5b06594
ACS Appl. Mater. Interfaces 2015, 7, 20460−20468

Cancer in Patients with Prior Negative Transrectal Ultrasound Biopsies. *J. Urol.* **2012**, *188*, 2152−2157.
(8) Brock, M.; Loppenberg, B.; Roghmann, F.; Pelzer, A.; Dickmann, M.; Becker, W.; Martin-Seidel, P.; Sommerer, F.; Schenk, L.; Palisaar, R. J.; Noldus, J.; von Bodman, C. Impact of Real-Time Elastography on Magnetic Resonance Imaging/Ultrasound Fusion Guided Biopsy in Patients with Prior Negative Prostate Biopsies. *J. Urol.* **2015**, *193*, 1191−1197.
(9) Du, Q. J.; Ma, T. C.; Fu, C. H.; Liu, T. L.; Huang, Z. B.; Ren, J.; Shao, H. B.; Xu, K.; Tang, F. Q.; Meng, X. W. Encapsulating Ionic Liquid and Fe_3O_4 Nanoparticles in Gelatin Microcapsules as Microwave Susceptible Agent for MR Imaging-guided Tumor Thermotherapy. *ACS Appl. Mater. Interfaces* **2015**, *7*, 13612−13619.
(10) Yang, F.; Wang, Q.; Gu, Z. X.; Fang, K.; Marriott, G.; Gu, N. Silver Nanoparticle-Embedded Microbubble as a Dual-Mode Ultrasound and Optical Imaging Probe. *ACS Appl. Mater. Interfaces* **2013**, *5*, 9217−9223.
(11) Gao, D.; Xu, M.; Cao, Z.; Gao, J. B.; Chen, Y.; Li, Y. Q.; Yang, Z.; Xie, X. Y.; Jiang, Q.; Wang, W.; Liu, J. Ultrasound-Triggered Phase-Transition Cationic Nanodroplets for Enhanced Gene Delivery. *ACS Appl. Mater. Interfaces* **2015**, *7*, 13524−13537.
(12) Zhang, B. B.; Li, Q.; Yin, P. H.; Rui, Y. P.; Qiu, Y. Y.; Wang, Y.; Shi, D. L. Ultrasound-Triggered BSA/SPION Hybrid Nanoclusters for Liver-Specific Magnetic Resonance Imaging. *ACS Appl. Mater. Interfaces* **2012**, *4*, 6479−6486.
(13) Mozer, P.; Rouprêt, M.; Le Cossec, C.; Granger, B.; Comperat, E.; de Gorski, A.; Cussenot, O.; Renard-Penna, R. First Round of Targeted Biopsies Using Magnetic Resonance Imaging/Ultrasonography Fusion Compared with Conventional Transrectal Ultrasonography-Guided Biopsies for the Diagnosis of Localised Prostate Cancer. *BJU Int.* **2015**, *115*, 50−57.
(14) Warlick, C. A. Multiparametric MRI for Prostate Cancer: Seeing Is Believing. *Cancer* **2014**, *120*, 2806−2809.
(15) Levens, E. D.; Wesley, R.; Premkumar, A.; Blocker, W.; Nieman, L. K. Magnetic Resonance Imaging and Transvaginal Ultrasound for Determining Fibroid Burden: Implications for Research and Clinical Care. *Am. J. Obstet. Gynecol.* **2009**, *200*, 537.e1−537.e7.
(16) Ferrara, K. W.; Borden, M. A.; Zhang, H. Lipid-Shelled Vehicles: Engineering for Ultrasound Molecular Imaging and Drug Delivery. *Acc. Chem. Res.* **2009**, *42*, 881−892.
(17) Shin, T. H.; Choi, Y.; Kim, S.; Cheon, J. Recent Advances in Magnetic Nanoparticle-based Multi-modal Imaging. *Chem. Soc. Rev.* **2015**, *44*, 4501.
(18) Singh, A.; Dilnawaz, F.; Mewar, S.; Sharma, U.; Jagannathan, N. R.; Sahoo, S. K. Composite Polymeric Magnetic Nanoparticles for Co-Delivery of Hydrophobic and Hydrophilic Anticancer Drugs and MRI Imaging for Cancer Therapy (Retracted article. See vol. 6, pg. 4595, 2014). *ACS Appl. Mater. Interfaces* **2011**, *3*, 842−856.
(19) An, L.; Hu, H.; Du, J.; Wei, J.; Wang, L.; Yang, H.; Wu, D. M.; Shi, H. L.; Li, F. H.; Yang, S. P. Paramagnetic Hollow Silica Nanospheres for in Vivo Targeted Ultrasound and Magnetic Resonance Imaging. *Biomaterials* **2014**, *35*, 5381−5392.
(20) Song, S.; Guo, H. Z.; Jiang, Z. Q.; Jin, Y. Q.; Zhang, Z. F.; Sun, K.; Dou, H. J. Self-Assembled Fe_3O_4/Polymer Hybrid Microbubble with MRI/Ultrasound Dual-Imaging Enhancement. *Langmuir* **2014**, *30*, 10557−10561.
(21) Brismar, T. B.; Grishenkov, D.; Gustafsson, B.; Harmark, J.; Barrefelt, A.; Kothapalli, S. V. V. N.; Margheritelli, S.; Oddo, L.; Caidahl, K.; Hebert, H.; Paradossi, G. Magnetite Nanoparticles Can Be Coupled to Microbubbles to Support Multimodal Imaging. *Biomacromolecules* **2012**, *13*, 1390−1399.
(22) Feshitan, J. A.; Boss, M. A.; Borden, M. A. Magnetic Resonance Properties of Gd(III)-bound Lipid-coated Microbubbles and Their Cavitation Fragments. *Langmuir* **2012**, *28*, 15336−15343.
(23) Park, J. I.; Jagadeesan, D.; Williams, R.; Oakden, W.; Chung, S. Y.; Stanisz, G. J.; Kumacheva, E. Microbubbles Loaded with Nanoparticles: A Route to Multiple Imaging Modalities. *ACS Nano* **2010**, *4*, 6579−6586.
(24) Yang, P.; Wang, F.; Luo, X. F.; Zhang, Y. T.; Guo, J.; Shi, W. B.; Wang, C. C. Rational Design of Magnetic Nanorattles as Contrast Agents for Ultrasound/Magnetic Resonance Dual-Modality Imaging. *ACS Appl. Mater. Interfaces* **2014**, *6*, 12581−12587.
(25) Fan, C. H.; Ting, C. Y.; Lin, H. J.; Wang, C. H.; Liu, H. L.; Yen, T. C.; Yeh, C. K. SPIO-conjugated, Doxorubicin-loaded Microbubbles for Concurrent MRI and Focused-ultrasound Enhanced Brain-tumor Drug Delivery. *Biomaterials* **2013**, *34*, 3706−3715.
(26) Yang, F.; Li, Y. X.; Chen, Z. P.; Zhang, Y.; Wu, J. R.; Gu, N. Superparamagnetic Iron Oxide Nanoparticle-embedded Encapsulated Microbubbles as Dual Contrast Agents of Magnetic Resonance and Ultrasound Imaging. *Biomaterials* **2009**, *30*, 3882−3890.
(27) Liu, Z.; Lammers, T.; Ehling, J.; Fokong, S.; Bornemann, J.; Kiessling, F.; Gatjens, J. Iron Oxide Nanoparticle-containing Microbubble Composites as Contrast Agents for MR and Ultrasound Dual-modality Imaging. *Biomaterials* **2011**, *32*, 6155−6163.
(28) Huang, H. Y.; Hu, S. H.; Hung, S. Y.; Chiang, C. S.; Liu, H. L.; Chiu, T. L.; Lai, H. Y.; Chen, Y. Y.; Chen, S. Y. SPIO Nanoparticle-stabilized PAA-F127 Thermosensitive Nanobubbles with MR/US Dual-modality Imaging and HIFU-triggered Drug Release for Magnetically Guided in Vivo Tumor Therapy. *J. Controlled Release* **2013**, *172*, 118−127.
(29) Niu, C. C.; Wang, Z. G.; Lu, G. M.; Krupka, T. M.; Sun, Y.; You, Y. F.; Song, W. X.; Ran, H. T.; Li, P.; Zheng, Y. Y. Doxorubicin Loaded Superparamagnetic PLGA-iron Oxide Multifunctional Microbubbles for Dual-mode US/MR Imaging and Therapy of Metastasis in Lymph Nodes. *Biomaterials* **2013**, *34*, 2307−2317.
(30) Sun, Y.; Zheng, Y. Y.; Ran, H. T.; Zhou, Y.; Shen, H. X.; Chen, Y.; Chen, H. R.; Krupka, T. M.; Li, A.; Li, P.; Wang, Z. B.; Wang, Z. G. Superparamagnetic PLGA-iron Oxide Microcapsules for Dual-modality US/MR Imaging and High Intensity Focused US Breast Cancer Ablation. *Biomaterials* **2012**, *33*, 5854−5864.
(31) Ao, M.; Wang, Z. G.; Ran, H. T.; Guo, D. J.; Yu, J. H.; Li, A.; Chen, W. J.; Wu, W.; Zheng, Y. Y. Gd-DTPA-loaded PLGA Microbubbles as Both Ultrasound Contrast Agent and MRI Contrast Agent-A Feasibility Research. *J. Biomed. Mater. Res., Part B* **2010**, *93B*, 551−556.
(32) Zhao, Y. J.; Song, W. X.; Wang, D.; Ran, H. T.; Wang, R. H.; Yao, Y. Z.; Wang, Z. G.; Zheng, Y. Y.; Li, P. Phase-Shifted PFH@PLGA/Fe_3O_4 Nanocapsules for MRI/US Imaging and Photothermal Therapy with near-Infrared Irradiation. *ACS Appl. Mater. Interfaces* **2015**, *7*, 14231−14242.
(33) Cheng, L.; Gong, H.; Zhu, W. W.; Liu, J. J.; Wang, X. Y.; Liu, G.; Liu, Z. PEGylated Prussian Blue Nanocubes as A Theranostic Agent for Simultaneous Cancer Imaging and Photothermal Therapy. *Biomaterials* **2014**, *35*, 9844−9852.
(34) Liu, X. S.; Huang, N.; Li, H.; Wang, H. B.; Jin, Q.; Ji, J. Multidentate Polyethylene Glycol Modified Gold Nanorods for in Vivo Near-Infrared Photothermal Cancer Therapy. *ACS Appl. Mater. Interfaces* **2014**, *6*, 5657−5668.
(35) Loh, X. J.; Ong, S. J.; Tung, Y. T.; Choo, H. T. Incorporation of Poly[(R)-3-hydroxybutyrate] into Cationic Copolymers Based on Poly(2-(dimethylamino)ethyl methacrylate) to Improve Gene Delivery. *Macromol. Biosci.* **2013**, *13*, 1092−1099.
(36) Loh, X. J.; Ong, S. J.; Tung, Y. T.; Choo, H. T. Dual Responsive Micelles Based On Poly[(R)-3-hydroxybutyrate] and Poly(2-(dimethylamino)ethyl methacrylate) for Effective Doxorubicin Delivery. *Polym. Chem.* **2013**, *4*, 2564−2574.
(37) Kai, D.; Loh, X. J. Polyhydroxyalkanoates: Chemical Modifications Toward Biomedical Applications. *ACS Sustainable Chem. Eng.* **2014**, *2*, 106−119.
(38) Li, Z. B.; Loh, X. J. Water Soluble Polyhydroxyalkanoates: Future Materials for Therapeutic applications. *Chem. Soc. Rev.* **2015**, *44*, 2865−2879.
(39) Liu, B. X.; Zhou, X.; Yang, F.; Shen, H.; Wang, S. G.; Zhang, B.; Zhi, G.; Wu, D. C. Fabrication of Uniform Sized Polylactone Microcapsules by Premix Membrane Emulsification for Ultrasound Imaging. *Polym. Chem.* **2014**, *5*, 1693−1701.

DOI: 10.1021/acsami.5b06594
ACS Appl. Mater. Interfaces 2015, 7, 20460−20468

(40) Shen, H.; Niu, Y. G.; Hu, X. X.; Yang, F.; Wang, S. G.; Wu, D. C. A Biomimetic 3D Microtubule-orientated Poly(lactide-co-glycolide) Scaffold with Interconnected Pores for Tissue Engineering. *J. Mater. Chem. B* **2015**, *3*, 4417−4425.
(41) Huang, D.; Li, D. W.; Wang, T. T.; Shen, H.; Zhao, P.; Liu, B.; You, Y. Z.; Ma, Y. Z.; Yang, F.; Wu, D. C.; Wang, S. G. Isoniazid Conjugated Poly(lactide-co-glycolide): Long-term Controlled Drug Release and Tissue Regeneration for Bone Tuberculosis Therapy. *Biomaterials* **2015**, *52*, 417−425.
(42) Sun, S. H.; Zeng, H.; Robinson, D. B.; Raoux, S.; Rice, P. M.; Wang, S. X.; Li, G. X. Monodisperse MFe_2O_4 (M = Fe, Co, Mn) Nanoparticles. *J. Am. Chem. Soc.* **2004**, *126*, 273−279.
(43) Hao, R.; Xing, R. J.; Xu, Z. C.; Hou, Y. L.; Gao, S.; Sun, S. H. Synthesis, Functionalization, and Biomedical Applications of Multifunctional Magnetic Nanoparticles. *Adv. Mater.* **2010**, *22*, 2729−2742.
(44) Yang, P.; Zhao, F. Y.; Ding, J.; Guo, J.; Shi, W. B.; Wang, C. C.; Hu, X. H. Bubble-in-Bubble Strategy for High-Quality Ultrasound Imaging with A Structure Coupling Effect. *Chem. Mater.* **2014**, *26*, 2121−2127.
(45) Arbab, A. S.; Yocum, G. T.; Kalish, H.; Jordan, E. K.; Anderson, S. A.; Khakoo, A. Y.; Read, E. J.; Frank, J. A. Efficient Magnetic Cell Labeling with Protamine Sulfate Complexed to Ferumoxides for Cellular MRI. *Blood* **2004**, *104*, 1217−1223.
(46) Jokerst, J. V.; Gambhir, S. S. Molecular Imaging with Theranostic Nanoparticles. *Acc. Chem. Res.* **2011**, *44*, 1050−1060.

DOI: 10.1021/acsami.5b06594
ACS Appl. Mater. Interfaces 2015, 7, 20460−20468